Hydrodeoxygenation of anisole over Pt/Al-SBA-15: metal-acid synergy

Atal Shivhare[1], James A. Hunns,[1] Lee J. Durndell,[2] Christopher M. A. Parlett,[3,4] Mark A. Isaacs,[5,6] Adam F. Lee[7] and Karen Wilson[7*]*

[1]European Bioenergy Research Institute, Aston University, Birmingham B4 7ET, UK

[2]School of Geography, Earth and Environmental Sciences, University of Plymouth, Plymouth PL4 8AA, UK

[3]School of Chemical Engineering and Analytical Science, University of Manchester, Manchester M13 9PL, UK

[4]University of Manchester at Harwell, Diamond Light Source, Harwell Science and Innovation Campus, Didcot OX11 0DE, UK

[5]Department of Chemistry, University College London, London, WC1H 0AJ, UK

[6]HarwellXPS, Research Complex at Harwell, Rutherford Appleton Laboratories, Didcot, OX11 0FA

[7]Applied Chemistry & Environmental Science, RMIT University, Melbourne VIC3000, Australia

KEYWORDS Catalysis, biofuels, hydrodeoxygenation, Al-SBA-15, platinum

ABSTRACT

Hydrodeoxygenation (HDO) is a promising technology to upgrade fast pyrolysis bio-oils but requires active and selective catalysts. Here we explore the synergy between metal and acid sites in the HDO of anisole, a model pyrolysis bio-oil compound, over mono- and bifunctional Pt/(Al)-SBA-15 catalysts. Ring hydrogenation of anisole to methoxycyclohexane occurs over metal sites and is structure sensitive, being favored over small (4 nm) Pt nanoparticles which confer a turnover frequency (TOF) of ~2000 h^{-1} and methoxycyclohexane selectivity of ~90 % at 200 °C and 20 bar H_2; in contrast, formation of benzene and the desired cyclohexane product appears structure insensitive. Introduction of acidity to the SBA-15 support promotes demethyoxylation of the methoxycyclohexane intermediate, increasing the selectivity to cyclohexane from 15 % to 92 % and 6 h cyclohexane productivity by two orders of magnitude (from 15 $mmol.g_{Pt}^{-1}.h^{-1}$ to 6500 $mmol.g_{Pt}^{-1}.h^{-1}$). Optimizing the metal-acid synergy confers an 865-fold increase in cyclohexane production per gram Pt and 28-fold reduction in precious metal loading. These findings demonstrate that tuning the metal-acid synergy provides a strategy to direct complex catalytic reaction networks and minimize precious metal use in biofuels production.

INTRODUCTION

Anthropogenic CO_2 contributions to atmospheric greenhouse gases, arising from fossil fuel combustion, have triggered a global socio-political movement seeking renewable and sustainable energy alternatives.[1, 2] Lignocellulose, derived from agricultural waste, is viewed as a potential sustainable carbon source to produce renewable transportation fuels and chemicals.[3] Fast pyrolysis, at moderate temperature (~450-550 °C) and short residence time, is an efficient route to produce high yields of liquid bio-oil from lignocellulosic biomass,[4, 5] which retain up to 70 % of

the original lignocellulose energy content.[3] However, the high oxygen content of fast pyrolysis bio-oil, associated with carbonyl, carboxylic acid and phenolic components, alongside reactive small oxygenates and water, destabilizes pyrolysis bio-oil, lowering its energy density compared to fossil petroleum fuels. Bio-oils are consequently unsuitable as a drop-in replacement fuel for gasoline, diesel or kerosene and require catalytic upgrading to neutralize reactive acids and carbonyls to produce more stable bio-oils with improved energy density.[6,7,8] Stabilized bio-oils contain between 10 % to 30 % aromatic compounds including syringyl, guaiacyl and other phenolics depending on the biomass source,[9] which require hydrodeoxygenation (HDO) of respective alcohol and ether functions to produce gasoline range hydrocarbons.[10,11,12]

Bio-oil HDO can be performed over sulfided NiMo/CoMo catalysts, however the high oxygen content of bio-oils necessitates the continuous addition of organic S compounds to maintain catalyst activity,[23] hence robust non-sulfided catalysts are sought for biomass-to-fuels.[13, 14] A range of supported transition metals have been explored for catalytic HDO. Neutral and Lewis acidic supports[15-18] require high temperature and H_2 pressure (>300 °C and >50 bar) to achieve deoxygenation, resulting in short catalyst lifetimes through coking and sintering and poor process economics. High HDO reaction temperatures also shift the thermodynamic equilibrium towards aromatics versus the desired ring-hydrogenated products.[19] Bifunctional catalysts comprising noble metal nanoparticles and Brønsted acidic supports are thus preferred for HDO,[19] enabling operation under milder conditions (e.g. 250 °C and 40 bar H_2 for guaiacol HDO over Pt/HY).[20] However, despite many reports of bifunctional catalysts for bio-oil HDO,[21, 19, 22 23] a significant knowledge gap remains regarding the metal-acid synergy due to a lack of systematic studies, with arbitrary combinations of metals (e.g. Pd, Pt, Ru) and acids (e.g. sulfated zirconia, Amberlyst-15, Nafion, zeolites, polyoxometallates, phosphoric acid and triflates)[21, 24-27] often employed at high

(1-5 wt%) precious metal loadings. Unravelling the complex interdependent interactions between metal and acid sites in HDO remains challenging.

Previous mechanistic studies suggest that the metal catalyzed hydrogenation of aromatic oxygenates occurs prior to deoxygenation over Brønsted acid sites under mild conditions (150-250 °C and 20-50 bar H_2 which offer enhanced catalyst lifetimes).[28-30 31 32] Phenol HDO over Pd/MoO_3-P_2O_5/SiO_2 at 112 °C and 10 bar H_2 is reported to proceed via hydrogenation to cyclohexanol over highly dispersed Pd nanoparticles, followed by cyclohexanol dehydration to cyclohexene over the m-MoO_3-P_2O_5 support and subsequent Pd catalyzed cyclohexene hydrogenation to cyclohexane.[29] A similar mechanism is advanced for phenol HDO over Ru/HZSM-5 at 200°C and 50 bar H_2,[30] and 1 wt% Pt/sulfonic acid-SBA-15.[33] Guaiacol HDO is also reported at 250 °C and 50 bar H_2 over bifunctional catalysts including Pd, Rh, Ru, and Pt supported on Al_2O_3, Al_2O_3-SiO_2, and nitric-acid-treated carbon black (NAC) supports.[31] Under these conditions, metal sites appear responsible for guaiacol hydrogenation to 2-methoxycyclohexanol, with subsequent deoxygenation to cyclohexane occurring over the acidic support. The superior activity of Pt/Al-SBA-15 for guaiacol HDO versus Pt/HZSM-5 is attributed to the larger pore diameter of the former, highlighting the importance of in-pore mass transport.[23] Pt/TiO_2[34] also shows promise for guaiacol hydrogenation at 280 °C and 10 bar H_2, but a Pt loading ≥2 wt% was deemed necessary for efficient ring hydrogenation. Despite these studies, the detailed reaction sequence for guaiacol HDO remains unclear due to competing pathways[35,36] and limited efforts to quantify the roles of acid and metal on alcohol/ether deoxygenation and ring hydrogenation respectively.

Anisole, containing only an aryl methyl ether group, is a useful model for phenolic residues obtained from lignin depolymerization during fast pyrolysis. Anisole HDO occurs through competing pathways,[20, 37, 38] depending on the reaction conditions employed, with high

temperatures of 300-500 °C typical.[21, 37, 39, 40] Under low pressure and high temperature conditions (1 bar H_2 and 375 °C) continuous flow anisole HDO over 1 wt% Pt/SiO_2 forms benzene as the dominant product via demethylation to a phenol intermediate.[40] Comparison of 1.7 wt% Pt supported on SiO_2, γ-Al_2O_3, Na-Beta, and NaH-Beta catalysts for anisole HDO (1 bar H_2 and 400 °C) revealed little synergy between metal and acid sites, with [phenol+benzene] yields <50 % and only trace methoxycyclohexane/cyclohexane.[37] Likewise over 1 wt% Pt/H-Beta under the same conditions, anisole is also reported to undergo transalkylation and demethylation reactions to cresol and phenol respectively rather than HDO.[21] Monometallic Pt and bimetallic core-shell Mo@Pt catalysts supported on SiO_2-Al_2O_3 also exhibited poor activity for anisole HDO at 450 °C favoring transalkylation and demethylation products (phenol and cresol).[41] In contrast high pressure, moderate temperature (52 bar H_2 and 200 °C) conditions for anisole HDO over 5 wt% Pd/USY yields predominately cyclohexane (produced via a methoxycyclohexane intermediate), but with only a 56 % selectivity.[38] Similar trends but lower activity were reported for USY supported 5wt% Ni and Ru catalysts. In contrast, anisole HDO over 0.5 wt% Pt/HY (40 bar H_2 and 250 °C) resulted in an increased 86 % selectivity to cyclohexane.[20]

Possible reaction pathways for anisole HDO are summarized in **Scheme 1**: low pressure, high temperature conditions favor aromatic products regardless of the support; high pressure, low temperature conditions favor ring hydrogenation and deoxygenation to cyclohexane over acidic supports, however the mechanism of this multi-step transformation has not been elucidated, and the synergy between metal and acid sites[42] not quantified and fully exploited.

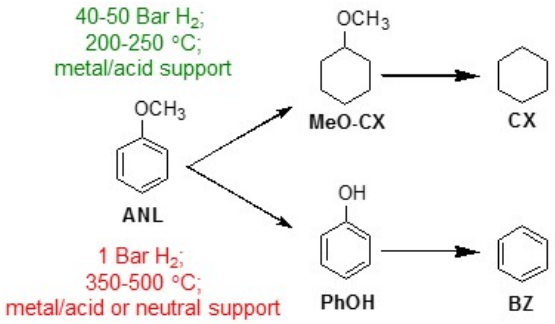

Scheme 1. Major reaction pathways for anisole hydrodeoxygenation.

Herein we investigate the respective roles of metal and acid sites, and their synergy, in anisole HDO over Pt/(Al)-SBA-15 catalysts. Small metal nanoparticles, derived using low (0.14 wt%) Pt loadings, act in concert with Brønsted acid sites to direct stepwise ring hydrogenation of anisole to methoxycyclohexane, demethoxylation to cyclohexene, and subsequent hydrogenation to the desired cyclohexane product. Tuning the metal-acid synergy promotes cyclohexane productivity by almost three orders of magnitude while simultaneously minimizing precious metal loading.

EXPERIMENTAL

Catalyst Synthesis

Mesoporous SBA-15 was prepared according to the literature.[43] Briefly, 10 g P123 was added to a polypropylene bottle, followed by 75 mL of deionized water. Subsequently, 250 mL of 2M HCl was added, and the resulting mixture stirred at 35 °C for 2.5 h until the P123 was fully solubilized. To this mixture, 23 mL of tetraethyl orthosilicate (TEOS) was added and stirring continued at 35 °C for a further 24 h. Hydrothermal aging was then conducted by placing the polypropylene bottle inside a drying oven at 80 °C for 24 h. The resulting solid was recovered by filtration, washed

repeatedly with deionized water, and subsequently calcined at 550 °C for 6 h under air (heating rate of 1°C.min^{-1}), and then cooled to room temperature and stored under air.

Al-SBA-15 was prepared according our previous reports using a true liquid crystal templating approach,[44, 45] by adding 2 g of P123, 0.7 g of $Al(NO_3)_3$, and 2g of 2M HCl to a 100 mL beaker (pH = 2), which was then immersed in an ultrasonic bath at 50 °C for 2 h to achieve a homogeneous mixture. To this, 4.1 mL of tetramethylorthosilicate (TMOS) was added under vigorous stirring until a smooth gel was obtained. The molar ratio of TMOS and $Al(NO_3)_3$ was adjusted so a total of 15 molar equivalent of TMOS was added to ensure a Si:Al ratio of 15:1. The gel was then transferred to a vacuum oven to remove the reactively-formed methanol at 40 °C under light vacuum (100 mbar) overnight. The resulting solid was recovered from the beaker and calcined at 550 °C for 5 h (heating rate of 1.5 °C.min^{-1}), cooled to room temperature and ground and sieved to a uniform particle size (sub-100 mesh). Additional Al-SBA-15 materials with Si:Al ratios of 6 to 67 was prepared for control experiments.

Pt nanoparticles were deposited on SBA-15 and Al-SBA-15 by wet impregnation of ammonium tetrachloroplatinate. 477.4 mg of $(NH_4)_2PtCl_4$ was dissolved in 50 mL deionized water (5 mg/mL of Pt). The required amount of this stock solution was transferred to a two-neck 100 mL round-bottomed flask containing the desired silica support to obtain two families of materials with Pt loadings spanning 0.14-4.44 wt% (SBA-15) and 0.16-9.54 wt% (Al-SBA-15). The final solution in each flask was topped up to 25 mL with deionized water, and the resulting slurry then stirred at room temperature overnight, and subsequently 50 °C for 4 days, until dry powder was obtained. The powders were recovered and calcined at 500 °C in a muffle furnace for 2 h (heating rate of 5 °C.min^{-1}), and subsequently reduced under flowing H_2 (15 mL.min^{-1}) in a tube furnace at 400 °C for 2 before cooling to room temperature. Samples were stored in air.

Catalyst characterisation

Elemental analysis was performed by inductively coupled plasma atomic emission spectroscopy (ICP-AES) using a Varian VISTA-AXCCD spectrophotometer (**Table 1**). Sample digestion was undertaken using an aqueous mixture of 2:1:1 HF/HNO_3/HCl. Textural properties of parent silicas and silica supported catalysts were obtained by N_2porosimetry at 77 K using a Nova 4000e Quantachrome porosimeter and NovaWin software version 11. Samples were degassed at 120 °C for 8 h prior to analysis. Pore diameter and volumes were calculated by applying the BJH method to the desorption isotherm, micropore areas were determined by t-plot analysis. Low and wide angle XRD patterns were recorded on a Bruker D8 Advance diffractometer equipped with a LynxEye high-speed strip detector Cu K_α (1.54 Å) radiation source, with a Ni filter, calibrated against a quartz standard. Low angle patterns were recorded from 2θ=0.3-8° with a step size of 0.01°, and wide angle patterns from 2θ=20-90° with a step size of 0.02°. Scherrer peak width analysis was used to estimate volume-averaged Pt crystallite diameters for Pt particles >5nm. For smaller Pt particles (< 5 nm) HRTEM imaging was performed on a JEOL 2100-F microscope operated at 200 kV, with image analysis using ImageJ 1.41 software. Samples for HRTEM analysis were prepared by dispersing the required amount in methanol, followed by drop casting on 100-mesh carbon coated copper grids, and drying at room temperature. Pt dispersions were measured via CO pulse chemisorption on a Quantachrome ChemBET 3000 chemisorption analyzer. Samples were degassed at 150 °C under flowing He for 1 h, prior to reduction at 200 °C under flowing H_2 (10 $mL.min^{-1}$) for 1 h before room temperature analysis. This reduction protocol is milder than that employed during Pt impregnation and does not induce particle sintering. A CO:Pt surface stoichiometry of 0.68 was assumed. Temperature-programmed desorption (TPD) measurements of acid properties were performed on a Mettler Toledo TGA/DS2 STAR analyzer linked to a

Pfeiffer Vacuum ThermoStar mass spectrometer (MS). For TPD measurements, 30 mg of catalysts were wet-impregnated with small amount of propylamine, and dried in a fume hood under lamellar flow, before drying in vacuum oven at 45 °C overnight. The impregnated catalysts were analyzed between 40 and 800 °C at a heating rate of 10 °C/min under flowing N_2 (30 ml/min). The evolved reactively-formed propene from propylamine decomposition was analyzed at m/Z = 41 using MS. DRIFTS measurements were performed using a Thermo Scientific Nicolet environmental cell and smart collector accessory and Thermo Scientific Nicolet iS50 FTIR spectrometer with MCT detector. The catalysts diluted with KBr (10 wt%) were wetted ex-situ with pyridine, and excess pyridine was removed overnight in vacuo at 40 °C. Prior to room temperature analysis, the catalysts were loaded in environmental cell and subjected to evacuation at 200 °C for 2 h under a He atmosphere to remove physisorbed water.

Hydrodeoxygenation reactions

Hydrodeoxygenation was performed in a 100 mL Parr 5500 Series stainless steel autoclave with a glass liner. In a typical reaction, the reactor was charged with the required amount of catalyst (50-300 mg as detailed in **Table S1**), 0.5 mL of n-tetradecane (Sigma-Aldrich, >99 %) as an internal standard, and 2 mmol anisole (Sigma-Aldrich, 99.7 %) in 50 mL n-dodecane (Sigma-Aldrich, >99 %) for Pt/SBA-15, or 5 mmol anisole in 50 mL n-dodecane for Pt/Al-SBA-15. Selected catalysts were also evaluated for phenol HDO using 100 mg catalyst, 5 mmol phenol (Sigma-Aldrich, >99 %) in 50 mL n-dodecane solvent, and methoxycyclohexane HDO using 25 mg catalyst, 10 mmol methoxycyclohexane (Sigma-Aldrich, >95 %), 50 mL n-dodecane solvent, 800 rpm, and 6 h reaction time. In all cases the reactor was sealed and purged three times with N_2 before heating to 200 °C under inert atmosphere. The reactor was subsequently pressurized with

20 bar H_2 and stirring (800 rpm) commenced. Aliquots (1 mL) were periodically withdrawn through a dip-tube and diluted 1:1 v/v with ethyl acetate before injection into a Varian 450GC fitted with a CP-Sil 5 CB column (15m x 0.32mm x 0.25µm) calibration. Reactivity parameters were calculated according to the equations below. Conversion was calculated using n_t as the reactant concentration at time t and n_0 as the initial reactant concentration. Selectivity was calculated for liquid phase products, where $n_{x=i}$ is the number of moles of product i, and Σn_x denotes the total amount of products detected. Mass-normalized initial rates were calculated at 20 % conversion, and corresponding turnover frequencies (TOFs) obtained by subsequent normalisation to the surface Pt concentration determined by CO chemisorption. The standard deviation in quoted values is ~3 %.

$\%\ \text{Conversion} = [(n_0 - n_t) / (n_0)] \times 100$

$\%\ \text{Selectivity} = [(n_{x=i}) / (\Sigma n_x)] \times 100$

$\%\ \text{Yield} = (\text{Conversion} \times \text{Selectivity}) / 100$

$\text{TOF} = \text{mmol}.h^{-1} / \text{mmol}Pt_{surface}$

Catalyst comparisons in this work are based on both rate data and 6 h yields, the latter account for potential differential deactivation over the course of reaction. Anisole conversion remained <80 % in all experiments (a consequence of our mild reaction temperature), mitigating potential bulk mass transport limitations.

RESULTS & DISCUSSION

Catalyst characterization

Preservation of the textural properties of the parent mesoporous SBA-15 and Al-SBA-15 silica supports following Pt impregnation was first verified by N_2 porosimetry; Type IV adsorption-desorption isotherms with H_1 hysteresis loops were observed for all materials (**Figure S1**) with corresponding BJH pore diameters of ~4.6±0.5 nm for Pt/SBA-15 and 3.6±0.4 nm for Pt/Al-SBA-15. BET surface areas fell for both SBA-15 and Al-SBA-15 following Pt impregnation (**Table 1**), attributed to micropore blockage for Pt/SBA-15 as evidenced by t-plot analysis. For Al-SBA-15, the micropore surface area was <5 % of the total surface area and hence the ~45% area loss following Pt impregnation suggests mesopore blockage by nanoparticles. TEM measurements of low loading Pt/SBA-15 revealed the presence of 3-6 nm particles aligned within the mesopore channels, as previously reported[46] (**Figure S2**); the largest particles, comparable to or exceeding the pore diameter, are likely present on the external surface. Smaller (1.5-3 nm) Pt nanoparticles were observed within the mesopore channels of Pt/Al-SBA-15 (**Figure S3**). Bulk and surface physicochemical properties are summarized in **Table 1**.

Low angle XRD revealed (100), (110), and (200) reflections characteristic of *P6mm* symmetry present within SBA-15[43] and Al-SBA-15[45] supports (**Figure S4**). These reflections were preserved in all corresponding Pt functionalized materials, indicating that the ordered hexagonal-close-packed (hcp) mesoporous architecture of both supports remained intact following Pt impregnation. Wide angle XRD of SBA-15 and Al-SBA-15 supported Pt catalysts exhibited reflections at 2θ = 39.9°, 46.2°, and 67.9°, corresponding to (111), (200), and (220) facets respectively of fcc Pt metal[46] (**Figure S5**). The peak width of Pt reflections decreased with metal loading for both supports, consistent with a fall in Pt dispersion calculated from CO chemisorption, corresponding

to Pt nanoparticle growth from 4→17 nm for SBA-15 and 2→34 nm for Al-SBA-15 (**Table 1**). Similar Pt loadings gave rise to smaller Pt nanoparticles for Al-SBA-15 in agreement with TEM, consistent with observations for Pd on alumina grafted SBA-15.[47]

The nature of acid sites was further probed by pyridine DRIFTS (**Figure 1**).[48] Unfunctionalized SBA-15 did not exhibit any adsorption bands characteristic of chemisorbed pyridine in accordance with the literature.[49] In contrast, Al-SBA-15 exhibited bands at 1447 cm^{-1} and 1597 cm^{-1} characteristic of pyridine adsorbed at Lewis acid sites arising from partially coordinated Al atoms (isomorphically substituted into the SBA-15 walls or extra-framework).[50] Additional bands at 1548 cm^{-1} and 1640 cm^{-1} are attributed to pyridinium ions adsorbed at Brønsted acid sites arising from Al substitution into the SBA-15 walls and associated charge balancing by protons. The remaining band at 1492 cm^{-1} is common to both the pyridinium ion and Lewis-bound pyridine. Platinum functionalization had minimal impact on the Brønsted:Lewis acid ratio on the Al-SBA-15 support.

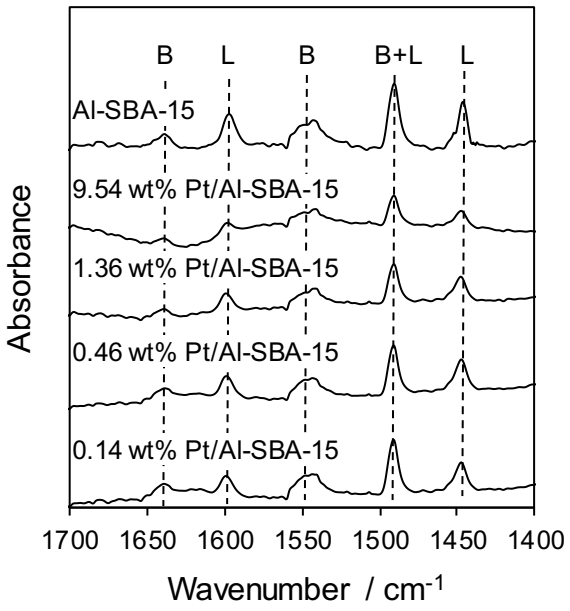

Figure 1. DRIFT spectra of chemisorbed pyridine over Pt/Al-SBA-15.

Table 1. Textural properties of SBA-15 and Al-SBA-15 supported Pt catalysts.

Support	Support Si:Al[a]	Nominal Pt loading / wt%	Actual Pt loading[a] / wt%	Pt dispersion[b] / %	Pt particle size[c,d] / nm	BET surface area[e] / m^2g^{-1}	Micropore surface area[e] / m^2g^{-1}	BJH pore diameter / nm[e]	Pore volume[e] / cm^3g^{-1}	Wall thickness[c] / nm	Acid site loading[f] / $mmolg^{-1}$
SBA-15	n/a	n/a	n/a	n/a	n/a	927 (±93)	328 (± 33)	4.7	0.93	5.7	n/a
SBA-15	n/a	5	4.44	7.7	17 (±2)[c]	714 (±71)	169 (± 17)	4.7	0.79	5.5	n/a
SBA-15	n/a	2	1.21	12.9	13 (±1)[c]	889 (±89)	173 (± 17)	4.7	1.03	6.7	n/a
SBA-15	n/a	1	0.88	13.6	11 (±1)[c]	624 (±62)	110 (± 11)	4.7	0.77	5.3	n/a
SBA-15	n/a	0.3	0.27	15.6	5 (±2)[d]	648 (±65)	182 (± 18)	4.7	0.69	5.3	n/a
SBA-15	n/a	0.2	0.14	19.2	4 (±2)[d]	492 (±49)	132 (± 13)	4.7	0.52	6.5	n/a
Al-SBA-15	14.5	n/a	n/a	n/a	n/a	443 (± 40)	33 (± 3)	3.6	0.44	6.0	0.34
Al-SBA-15	14.1	10	9.54	2.0	34 (± 3)[c]	254 (± 25)	0.0	3.6	0.78	5.8	0.18
Al-SBA-15	14.3	2	1.36	10.0	8 (± 1)[c]	273 (± 23)	0.0	3.6	0.34	5.9	0.16
Al-SBA-15	13.7	0.5	0.46	12.8	4 (±2)[d]	229 (± 23)	0.0	3.6	0.40	5.9	0.17
Al-SBA-15	14.0	0.2	0.16	18.6	2 (± 1)[d]	273 (± 27)	0.0	3.6	0.45	5.9	0.17

[a]ICP-AES;[b]CO chemisorption;[c]XRD;[d]TEM;[e]N_2 porosimetry;[f]TGA-MS

The total acid site density was quantified by titration with propylamine; the desorption temperatures of propene and ammonia reactively-formed by propylamine decomposition over acid sites also provide a qualitative measure of acid strength (**Figure S6**).[51] A common acid site loading of 0.17 mmol.g^{-1} was observed for all Pt/Al-SBA-15 materials, approximately half that of the parent Al-SBA-15. The propene desorption temperature was approximately 440 °C (indicative of moderate-strong acid sites[44, 52]) for Al-SBA-15 and Pt/Al-SBA-15 materials. In summary, the nature and strength of Al-SBA-15 support acidity was essentially independent of Pt functionalization.

Anisole hydrodeoxygenation:

Anisole HDO was first investigated over Pt/SBA-15 (**Figure S7a-b**). Specific activity per gram of Pt was inversely proportional to Pt particle size (**Figure 2**), however a significant deviation from linearity is observed, wherein rate $\propto$ diameter$^{-\gamma}$ with a proportionality constant $\gamma>1$. This indicates that activity was not directly correlated with the Pt surface atom density and hence that at least one of the potential competing routes for anisole conversion in **Scheme 1** is structure sensitive.[53, 54] This structure sensitivity is evidenced by the particle size dependence of turnover frequencies (TOFs) per surface Pt sites (determined by CO titration) wherein 4 nm particles were three times more active than 17 nm particles, reaching TOFs >2000 h^{-1} (compared to 1100 h^{-1} for Pd/C in water,[28] 4500 h^{-1} over Pt/SiO_2 at 375 °C in vapor flow and atmospheric pressure H_2[40] and 680 h^{-1} for Ni_2P/SiO_2 in liquid flow).[40] Structure sensitivity has also been observed in the solventless HDO of phenol over Ni/SiO_2,[55] however their TOFs for phenol hydrogenation were 85 times slower for 5 nm particles (40 h^{-1}) than for 22 nm particles (2300 h^{-1}) which may reflect the lower reducibility of nickel. [56] Note that benzene and toluene hydrogenation over Pt nanoparticles

are favored over smaller nanoparticles, possibly due to particle size dependency in reactant adsorption energies.[57, 58]

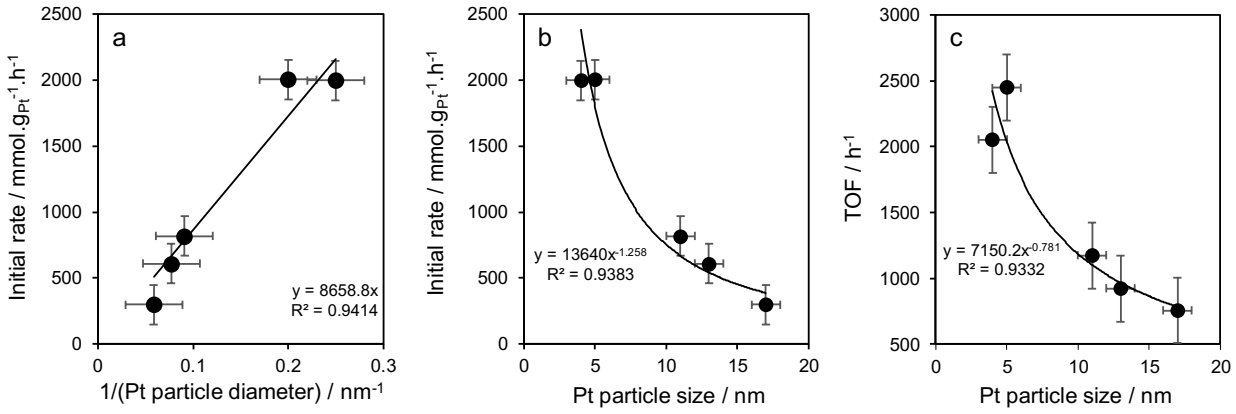

Figure 2. (a-b) Specific activity and (c) corresponding turnover frequency for anisole hydrodeoxygenation over Pt/SBA-15 catalysts as a function of Pt particle size. Reaction conditions: 200 °C; 20 bar H_2; 300 mg 0.14-0.27 wt% Pt/SBA-15 or 100 mg 0.88-4.44 wt% Pt/SBA-15; 2 mmol anisole; 50 mL dodecane solvent; and 800 rpm.

The observation that anisole conversion is structure sensitive implies that one (or more) of the resulting products should also exhibit structure sensitivity,[59, 60] and indeed the particle size dependent specific productivity of the ring-hydrogenated methoxycyclohexane mirrors that of anisole conversion, (**Figure 3**) consistent with the direct pathway indicated in **Scheme 1**. In contrast, the formation of benzene and cyclohexane minor products appears structure insensitive, suggesting that deoxygenation of their precursors must be rate-limiting, although their low concentrations make a definitive assessment difficult. The carbon mass balance was >85 % for all Pt/SBA-15 catalysts.

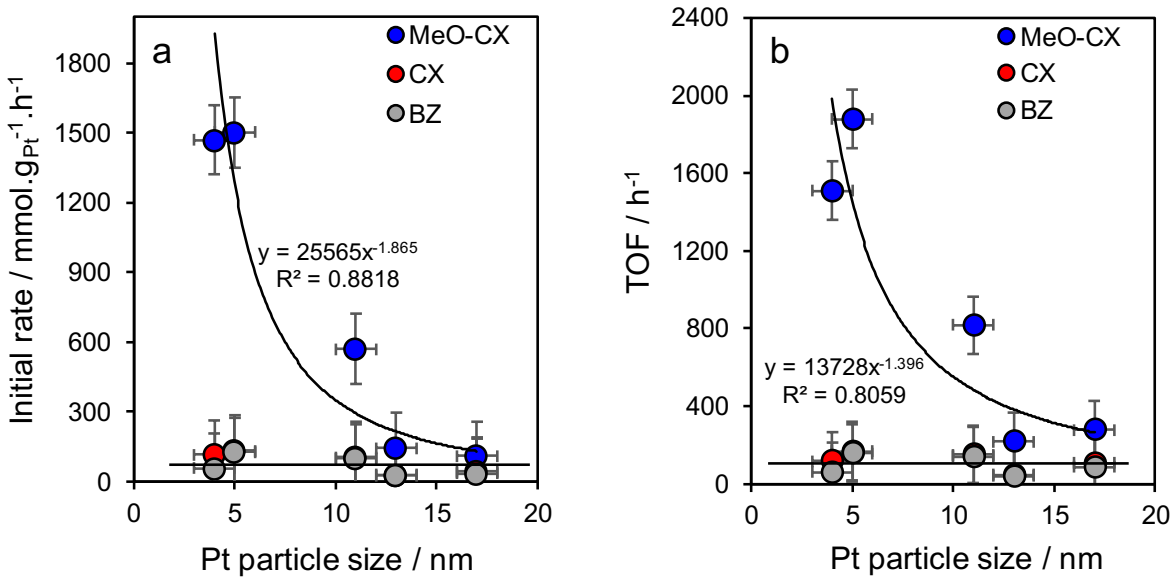

Figure 3. (a) Specific productivity and (b) corresponding turnover frequency of product formation for anisole hydrodeoxygenation over Pt/SBA-15 catalysts as a function of Pt particle size. Reaction conditions: 200 °C; 20 bar H_2; 300 mg 0.14-0.27 wt% Pt/SBA-15 or 100 mg 0.88-4.44 wt% Pt/SBA-15; 2 mmol anisole; 50 mL dodecane solvent; and 800 rpm.

The efficacy of small Pt particles for anisole HDO to methoxycyclohexane contrasts with that of phenol HDO over Ni/SiO_2[55] and 2-(2-methoxyphenoxy)-1-phenylethanol HDO over $Ru/NbOPO_4$[61] for which deoxygenation products dominate; this difference may be a consequence of the greater oxophilicity of Ni and Ru versus Pt,[62 63 64] and hence retention of Lewis acidic NiO_x and RuO_x sites under reaction conditions.[65 66, 67] Density functional theory (DFT) calculations and microkinetic analysis evidence that hydrogenation of the aromatic ring in phenolics is favored versus dissociation to benzene.[68] Selectivity to methoxycyclohexane over Pt/SBA-15 falls from ~90 % to 55 % as the particle size increased from 4 nm to 17 nm as a consequence of suppressed anisole hydrogenation (**Figure 4**). Benzene cannot originate from methoxycyclohexane, and hence must be produced by a distinct reaction pathway. Model single crystal experimental and DFT

studies indicate anisole can decompose via demethylation to phenol and subsequent deoxygenation to benzene via a 1,4-cyclohexadieneol intermediate.[69] Direct demethoxylation of anisole to benzene has also been invoked in the liquid phase,[70] although this reaction is thermodynamically unfavorable by 80-100 kJ mol^{-1} compared to demethylation.[71, 72] Cyclohexane may originate from either the demethoxylation of methoxycyclohexane or the hydrogenation of benzene.[57] As we discuss below, the former pathway dominates under our reaction conditions.

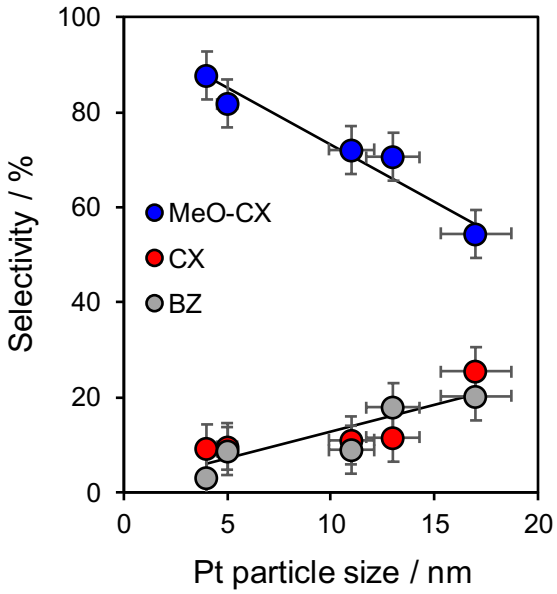

Figure 4. Selectivity at 20 % iso-conversion for anisole hydrodeoxygenation over Pt/SBA-15 catalysts as a function of Pt particle size. Reaction conditions: 200 °C; 20 bar H_2; 300 mg 0.14-0.27 wt% Pt/SBA-15 or 100 mg 0.88-4.44 wt% Pt/SBA-15; 2 mmol anisole; 50 mL dodecane solvent; and 800 rpm.

The significance of the demethoxylation pathway in anisole HDO was subsequently investigated by studying the reactivity of phenol over small (0.14 wt% Pt/SBA-15) and large (4.44 wt% Pt/SBA-15) Pt nanoparticles (**Figure S7c-d**). Specific activity for phenol HDO was between 20 and 140 times greater than that for anisole HDO (**Figure 5a**), however the reverse structure

sensitivity was observed with the TOF increasing from 54,000 h^{-1} to 106,000 h^{-1} from 4 to 17 nm particles (in accordance with phenol hydrogenation over Pt/C[73] and m-cresol HDO over Pt/TiO_2[74]). Note that average cyclohexane productivity from anisole over 6 h was only 8 mmol.g_{Pt}^{-1}.h^{-1} for the high loading Pt/SBA-15 catalyst.

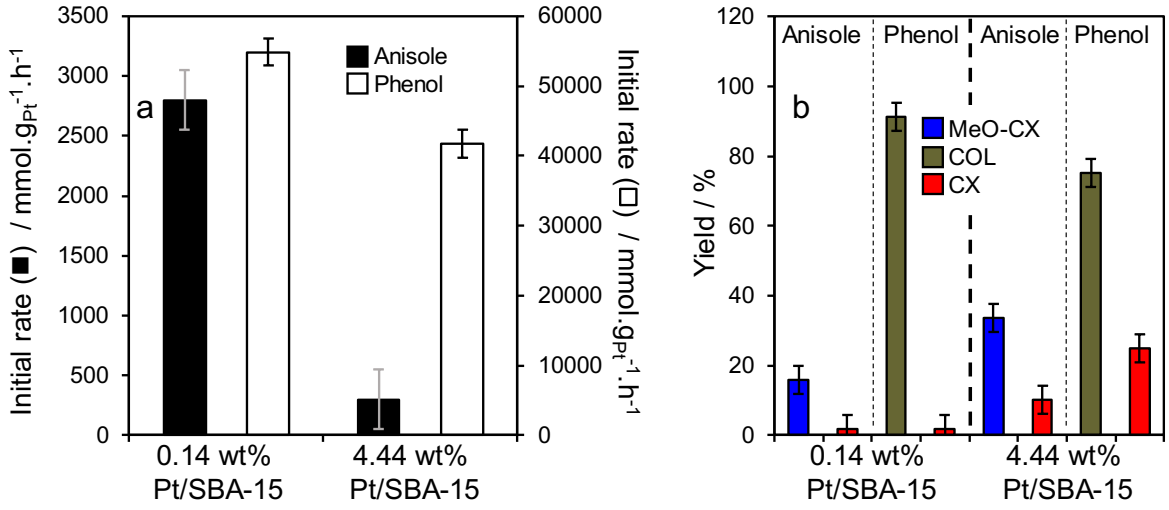

Figure 5. Comparison of (a) specific activity and (b) 6 h product yields for anisole and phenol HDO over 0.14 wt% Pt/SBA-15 and 4.44 wt% Pt/SBA-15 catalysts. Reaction conditions: 200 °C, 20 bar H2; 300 mg 0.14 wt% Pt/SBA-15 for anisole or 100 mg 0.14 wt% Pt/SBA-15 for phenol or 100 mg 4.44 wt% Pt/SBA-15 for anisole and phenol; 2 mmol anisole or 5 mmol phenol; 50 mL dodecane solvent; and 800 rpm.

Ring hydrogenation was the dominant pathway in phenol HDO, with cyclohexanol yields exceeding 75 % for both Pt/SBA-15 catalysts (**Figure 5b**); this contrasts with anisole HDO wherein negligible reactively-formed cyclohexanol was observed. We therefore conclude that demethylation is only a minor pathway in anisole HDO. In common with anisole HDO, yields of the minority deoxygenation products of phenol HDO (cyclohexane and benzene) increased with Pt particle size.

The preceding results demonstrate that Pt is effective for ring hydrogenation of anisole (and phenol) but ineffective for deoxygenation, consistent with literature for metal-only catalyzed HDO. [28 71 75] Introduction of acidity into the silica support dramatically enhanced both the specific activity for anisole HDO and the yield of desired cyclohexane product (**Figure 6** and **Figure S8**), although a similar size dependence was observed for Pt/Al-SBA-15 as for Pt/SBA-15 (**Figure S9**). The TOF for 0.16 wt% Pt/Al-SBA-15 was 67740 h^{-1} per Pt site or 621 h^{-1} per H^+, comparing very favorably with 10,700 h^{-1} for Pd/USY (200 °C and 52 bar H_2),[38] ~10,000 h^{-1} for 0.5 wt% Pt/HY(2.6) (250 °C and 40 bar H_2),[20] and 424 h^{-1} for Ni_2P/SiO_2 (300 °C and 15 bar H_2).[76] Such promotion may either reflect a new (facile) reaction pathway for anisole, such as transalkylation, demethylation,[20, 37, 77] or hydrolysis,[78] or the suppression of poisoning of Pt active sites by reaction intermediates formed over Pt/SBA-15. Since the same products are observed for Pt/Al-SBA-15 and Pt/SBA-15 (methoxycyclohexane, cyclohexane and benzene), we can infer that the former scenario is improbable, whereas experimental and theoretical studies over model Pt catalysts suggest that anisole is indeed prone to decomposition to strongly chemisorbed species (consistent with the latter scenario).[69, 79-81] The strong synergy between Pt and Brønsted acid sites confers a several hundredfold increase in average cyclohexane productivity over 6 h (from 15 $mmol.g_{Pt}^{-1}.h^{-1}$ to 6500 $mmol.g_{Pt}^{-1}h^{-1}$) for a common, low Pt loading, associated with a dramatic rate enhancement coupled with a sharp rise in cyclohexane selectivity (from 15 % to 92 %). Note that this synergy is significantly weaker for high metal loadings typically adopted in the literature, resulting in a smaller 6 h productivity enhancement (8 $mmol.g_{Pt}^{-1}.h^{-1}$ versus 161 $mmol.g_{Pt}^{-1}.h^{-1}$, see **Table S2**).

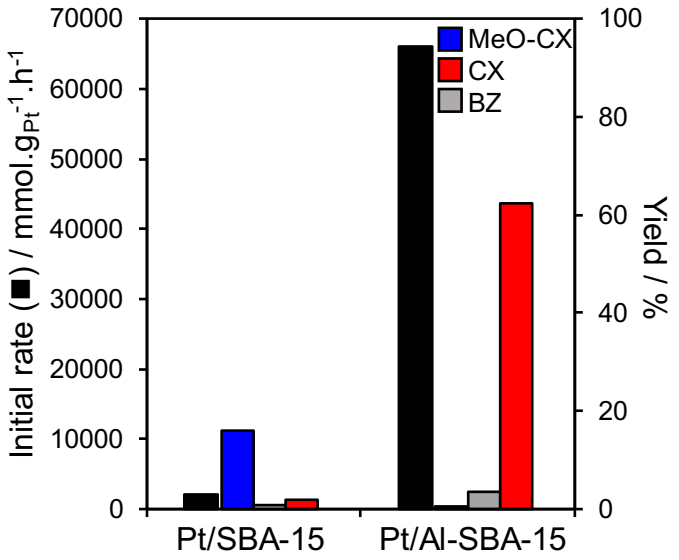

Figure 6. Comparison of specific activity and 6 h product yields for anisole HDO over 0.14 wt% Pt/SBA-15 versus 0.16 wt% Pt/Al-SBA-15. Reaction conditions: 200 °C; 20 bar H_2; 300 mg Pt/SBA-15 or 50 mg Pt/Al-SBA-15; 2 mmol anisole (Pt/SBA-15) or 5 mmol anisole (Pt/Al-SBA-15; 50 mL dodecane solvent; and 800 rpm.

To establish whether support acidity influences the deoxygenation of reactively-formed methoxycyclohexane, its reactivity was compared over the SBA-15 and Al-SBA-15, and Pt functionalized analogues (**Figure S10**). The parent Al-SBA-15 support was active for methoxycyclohexane demethoxylation to cyclohexene (presumably via dehydration of cyclohexanol)[82] whereas SBA-15 was inert (**Figure 7**), evidencing the significance of acid sites in ether HDO.[83] This can be rationalized based on acid sites promoting ether cleavage via protonation of the ether oxygen to form R-O(H^+)-R, followed by hydrolysis to R-OH species.[84] Pt addition to Al-SBA-15 promoted rapid cyclohexene hydrogenation to cyclohexane, but had little impact on the rate of methoxycyclohexane demethoxylation. Although Pt/SBA-15 showed some activity for methoxycyclohexane conversion, it was fully deactivated after 1 h reaction (**Figure S11**)

evidencing self-poisoning of metal sites; this is consistent with the accumulation of methoxycyclohexane during anisole HDO (as inferred in the preceding paragraph). A physical mixture containing 25 mg each of 0.14 wt% Pt/SBA-15 and Al-SBA-15 exhibited a cyclohexane productivity of only 148 mmol.g_{cat}^{-1}.h^{-1}, approximately half that of the bifunctional catalyst, demonstrating the importance of close proximity between metal and acid sites in maximizing HDO. Such proximity facilitates spillover of reactive intermediates to and from acid sites at the perimeter of metal nanoparticles,[85, 86] consistent with the observation that small Pt particles supported on Al-SBA-15 are optimal for HDO.

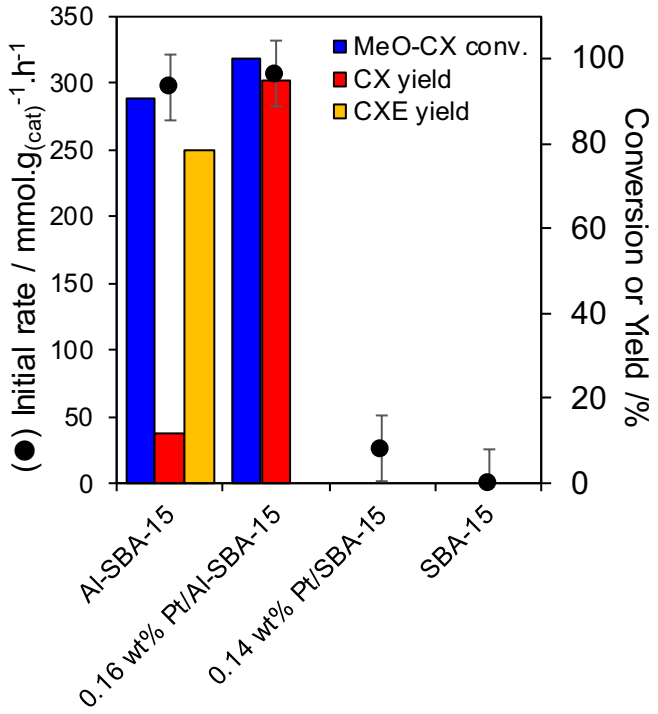

Figure 7. Comparison of activity, and 6 h conversion and product yields for methoxycyclohexane hydrodeoxygenation over SBA-15, Al-SBA-15 and Pt analogues. Reaction conditions: 200 °C; 20 bar H_2; 25 mg 0.14 wt% Pt/SBA-15 or 0.16 wt% Pt/Al-SBA-15; 10 mmol methoxycyclohexane; 50 mL n-dodecane solvent; and 800 rpm.

The amount and strength of acid sites will likely both influence anisole HDO, however independently varying these is challenging due to cooperative effects that emerge between neighbouring acid sites as their number is increased.[87, 88] Changing the solid acid support entirely to tune acid strength is problematic since metal dispersion and acid site accessibility are simultaneously changed.[24, 26] We therefore prepared a family of Al-SBA-15 supports of similar textural properties but different Al content (Si:Al ratios from 6 to 79). ^{27}Al MAS NMR and propylamine TPD analysis of Al-SBA-15 as a function of Si:Al ratio revealed an inverse relationship between the number of acid sites and their strength, associated with the formation of extra-framework alumina at very low Si:Al ratios (**Figure S12**). Stronger acid sites promote cyclohexanol deoxygenation, and hence the combination of higher Si:Al ratio supports with small Pt nanoparticles offers an interesting avenue for future research.

Anisole HDO over Pt/Al-SBA-15 thus proceeds through metal catalyzed ring hydrogenation to methoxycyclohexane, followed by acid catalyzed demethoxylation and dehydration to cyclohexene, and subsequent metal catalyzed hydrogenation of cyclohexene to cyclohexane as shown in **Scheme 2**. In the absence of support acidity, methoxycyclohexane accumulates on Pt sites possibly resulting in self-poisoning through decomposition products. Alternative reaction pathways, such as anisole demethylation to phenol or transalkylation to cresol, do not appear to operate, although the former may account for small amounts of reactively-formed benzene. Small Pt nanoparticles (formed at low Pt loadings) promote anisole hydrogenation, and their combination with Al-SBA-15 unlocks highly active and selective catalysts for anisole HDO to cyclohexane at moderate temperature (200 °C) and H_2 pressure (20 bar). Future work will explore the possibility of even greater precious metal thrifting[89] through extension to small Pt clusters (or single atoms[90]) in combination with hierarchically porous solid acid supports. Resasco and co-workers recently

reported that isolated Pt cations on a (moderate Lewis acid) TiO_2 support were less active than small Pt clusters for m-cresol HDO,[74] and future work will explore whether similar behaviour is observed for Brønsted acid supports.

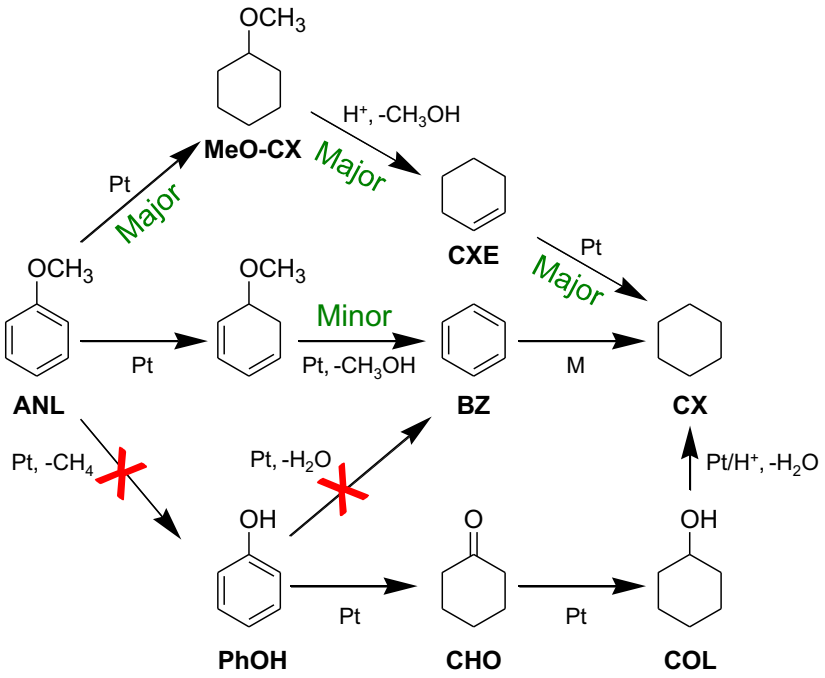

Scheme 2. Major reaction pathways for anisole hydrodeoxygenation over Pt/Al-SBA-15.

CONCLUSIONS

Anisole HDO to cyclohexane over bifunctional Pt/Al-SBA-15 catalysts proceeds via the stepwise (and structure sensitive) ring hydrogenation of anisole over Pt nanoparticles to methoxycyclohexane, demethoxylation over moderate-strong Brønsted acid sites to cyclohexene, and subsequent rapid hydrogenation over Pt to the desired cyclic alkane. Competing pathways for such as anisole demethylation to phenol or transalkylation to cresol are disfavored at the moderate reaction conditions (200 °C and 20 bar H_2) used in this study. A consequence of the preferential ring hydrogenation of anisole over small (≤4 nm) Pt nanoparticles, is that the optimum synergy

with neighboring acid sites occurs for metal loadings far lower than commonly adopted (≤0.16 wt% versus 1-5 wt%[19, 25-27]), conferring an 865-fold increase in cyclohexane production per gram Pt coupled with a 28-fold reduction in metal, exemplifying the concept of precious metal thrifting.

ASSOCIATED CONTENT

Supporting Information.

The following files are available free of charge.

AUTHOR INFORMATION

Corresponding Author

Adam F. Lee, adam.lee2@rmit.edu.au, +61 (0)399252623

Karen Wilson, karen.wilson2@rmit.edu.au, +61 (0)399252122

Author Contributions

The manuscript was written through contributions of all authors. All authors have given approval to the final version of the manuscript.

Funding Sources

We thank the EPSRC (EP/K036548/1 and EP/K014706/1) for financial support. JAH thanks Johnson Matthey for an Industrial CASE studentship. KW thanks the Royal Society for an Industry Fellowship. Support from the European Union Seventh Framework Programme (FP7/2007-2013) under grant agreement no. 604307 is also acknowledged).

REFERENCES

[1] C. Bessou, F. Ferchaud, B. Gabrielle, B. Mary *Agron Sustain Dev*. **2011**, *31*, 1-79.

[2] D. F. Dominkovic, I. Bacekovic, A. S. Pedersen, G. Krajacic *Renew Sust Energ Rev*. **2018**, *82*, 1823-1838.
[3] G. W. Huber, S. Iborra, A. Corma *Chem Rev*. **2006**, *106*, 4044-4098.
[4] D. Mohan, C. U. Pittman, P. H. Steele *Energy & Fuels*. **2006**, *20*, 848-889.
[5] D. Carpenter, T. L. Westover, S. Czernik, W. Jablonski *Green Chemistry*. **2014**, *16*, 384-406.
[6] A. A. Lappas, K. G. Kalogiannis, E. F. Iliopoulou, K. S. Triantafyllidis, S. D. Stefanidis *WIREs Energy and Environment*. **2012**, *1*, 285-297.
[7] L. Ciddor, J. A. Bennett, J. A. Hunns, K. Wilson, A. F. Lee *Journal of Chemical Technology & Biotechnology*. **2015**, *90*, 780-795.
[8] T. N. Pham, D. Shi, D. E. Resasco *Applied Catalysis B: Environmental*. **2014**, *145*, 10-23.
[9] L. Negahdar, A. Gonzalez-Quiroga, D. Otyuskaya, H. E. Toraman, L. Liu, J. T. B. H. Jastrzebski, K. M. Van Geem, G. B. Marin, J. W. Thybaut, B. M. Weckhuysen *ACS Sustain Chem Eng*. **2016**, *4*, 4974-4985.
[10] P. Mäki-Arvela, Y. D. Murzin *Catalysts*. **2017**, *7*.
[11] W. Jin, L. Pastor-Pérez, D. Shen, A. Sepúlveda-Escribano, S. Gu, T. Ramirez Reina *ChemCatChem*. **2019**, *11*, 924-960.
[12] S. Kim, E. E. Kwon, Y. T. Kim, S. Jung, H. J. Kim, G. W. Huber, J. Lee *Green Chemistry*. **2019**, *21*, 3715-3743.
[13] Y.-C. Lin, G. W. Huber *Energy & Environmental Science*. **2009**, *2*, 68-80.
[14] Z. Si, X. Zhang, C. Wang, L. Ma, R. Dong *Catalysts*. **2017**, *7*.
[15] Q. Bu, H. Lei, A. H. Zacher, L. Wang, S. Ren, J. Liang, Y. Wei, Y. Liu, J. Tang, Q. Zhang, R. Ruan *Bioresource Technology*. **2012**, *124*, 470-477.
[16] P. M. de Souza, R. C. Rabelo-Neto, L. E. P. Borges, G. Jacobs, B. H. Davis, D. E. Resasco, F. B. Noronha *ACS Catal*. **2017**, *7*, 2058-2073.
[17] C. A. Teles, R. C. Rabelo-Neto, G. Jacobs, B. H. Davis, D. E. Resasco, F. B. Noronha *Chemcatchem*. **2017**, *9*, 2850-2863.
[18] P. M. de Souza, R. C. Rabelo-Neto, L. E. P. Borges, G. Jacobs, B. H. Davis, U. M. Graham, D. E. Resasco, F. B. Noronha *ACS Catal*. **2015**, *5*, 7385-7398.
[19] A. M. Robinson, J. E. Hensley, J. W. Medlin *ACS Catal*. **2016**, *6*, 5026-5043.
[20] H. Lee, H. Kim, M. J. Yu, C. H. Ko, J.-K. Jeon, J. Jae, S. H. Park, S.-C. Jung, Y.-K. Park *Sci Rep*. **2016**, *6*, 28765-28765.
[21] X. Zhu, L. L. Lobban, R. G. Mallinson, D. E. Resasco *Journal of Catalysis*. **2011**, *281*, 21-29.
[22] H. W. Lee, B. R. Jun, H. Kim, D. H. Kim, J.-K. Jeon, S. H. Park, C. H. Ko, T.-W. Kim, Y.-K. Park *Energy*. **2015**, *81*, 33-40.
[23] M. J. Yu, S. H. Park, J.-K. Jeon, C. Ryu, J. M. Sohn, S. C. Kim, Y.-K. Park *Journal of Nanoscience and Nanotechnology*. **2015**, *15*, 527-531.
[24] C. Zhao, J. A. Lercher *ChemCatChem*. **2012**, *4*, 64-68.
[25] C. Zhao, Y. Kou, A. A. Lemonidou, X. Li, J. A. Lercher *Angewandte Chemie International Edition*. **2009**, *48*, 3987-3990.
[26] Q. Xia, Z. Chen, Y. Shao, X. Gong, H. Wang, X. Liu, S. F. Parker, X. Han, S. Yang, Y. Wang *Nature Communications*. **2016**, *7*, 11162.
[27] H. Wang, H. Wang, E. Kuhn, M. P. Tucker, B. Yang *ChemSusChem*. **2018**, *11*, 285-291.
[28] C. Zhao, J. Y. He, A. A. Lemonidou, X. B. Li, J. A. Lercher *Journal of Catalysis*. **2011**, *280*, 8-16.

[29] H. H. Duan, J. C. Dong, X. R. Gu, Y. K. Peng, W. X. Chen, T. Issariyakul, W. K. Myers, M. J. Li, N. Yi, A. F. R. Kilpatrick, Y. Wang, X. S. Zheng, S. F. Ji, Q. Wang, J. T. Feng, D. L. Chen, Y. D. Li, J. C. Buffet, H. C. Liu, S. C. E. Tsang, D. O'Hare *Nature Communications*. **2017**, *8*.
[30] W. Zhang, J. Z. Chen, R. L. Liu, S. P. Wang, L. M. Chen, K. G. Li *ACS Sustain Chem Eng*. **2014**, *2*, 683-691.
[31] C. R. Lee, J. S. Yoon, Y.-W. Suh, J.-W. Choi, J.-M. Ha, D. J. Suh, Y.-K. Park *Catalysis Communications*. **2012**, *17*, 54-58.
[32] A. Berenguer, J. A. Bennett, J. Hunns, I. Moreno, J. M. Coronado, A. F. Lee, P. Pizarro, K. Wilson, D. P. Serrano *Catalysis Today*. **2018**, *304*, 72-79.
[33] L. Mo, W. Yu, H. Cai, H. Lou, X. Zheng. **2018**, *6*.
[34] R. Shu, B. Lin, C. Wang, J. Zhang, Z. Cheng, Y. Chen *Fuel*. **2019**, *239*, 1083-1090.
[35] T. Nimmanwudipong, R. C. Runnebaum, D. E. Block, B. C. Gates *Energy & Fuels*. **2011**, *25*, 3417-3427.
[36] F. P. Bouxin, X. Zhang, I. N. Kings, A. F. Lee, M. J. H. Simmons, K. Wilson, S. D. Jackson *Organic Process Research & Development*. **2018**, *22*, 1586-1589.
[37] M. S. Zanuttini, C. D. Lago, M. S. Gross, M. A. Peralta, C. A. Querini *Industrial & Engineering Chemistry Research*. **2017**, *56*, 6419-6431.
[38] D. P. Gamliel, S. Karakalos, J. A. Valla *Applied Catalysis A: General*. **2018**, *559*, 20-29.
[39] H. Wang, M. Feng, B. Yang *Green Chemistry*. **2017**, *19*, 1668-1673.
[40] Q. Tan, G. Wang, A. Long, A. Dinse, C. Buda, J. Shabaker, D. E. Resasco *Journal of Catalysis*. **2017**, *347*, 102-115.
[41] Q. Lai, C. Zhang, J. H. Holles *Catalysis Science & Technology*. **2017**, *7*, 3220-3233.
[42] W. Luo, W. Cao, P. C. A. Bruijnincx, L. Lin, A. Wang, T. Zhang *Green Chemistry*. **2019**, *21*, 3744-3768.
[43] D. Zhao, J. Feng, Q. Huo, N. Melosh, G. H. Fredrickson, B. F. Chmelka, G. D. Stucky *Science*. **1998**, *279*, 548.
[44] K. B. Baharudin, Y. H. Taufiq-Yap, J. Hunns, M. Isaacs, K. Wilson, D. Derawi *Microporous and Mesoporous Materials*. **2019**, *276*, 13-22.
[45] K. B. Baharudin, M. Arumugam, J. Hunns, A. F. Lee, E. Mayes, Y. H. Taufiq-Yap, K. Wilson, D. Derawi *Catalysis Science & Technology*. **2019**, *9*, 6673-6680.
[46] L. J. Durndell, C. M. A. Parlett, N. S. Hondow, M. A. Isaacs, K. Wilson, A. F. Lee *Sci Rep*. **2015**, *5*, 9425.
[47] C. M. A. Parlett, L. J. Durndell, A. Machado, G. Cibin, D. W. Bruce, N. S. Hondow, K. Wilson, A. F. Lee *Catalysis Today*. **2014**, *229*, 46-55.
[48] Y. Matsunaga, H. Yamazaki, T. Yokoi, T. Tatsumi, J. N. Kondo *J Phys Chem C*. **2013**, *117*, 14043-14050.
[49] S.-Y. Chen, S. Lao-ubol, T. Mochizuki, Y. Abe, M. Toba, Y. Yoshimura *Applied Catalysis A: General*. **2014**, *485*, 28-39.
[50] Y. Matsunaga, H. Yamazaki, T. Yokoi, T. Tatsumi, J. N. Kondo *The Journal of Physical Chemistry C*. **2013**, *117*, 14043-14050.
[51] W. E. Farneth, R. J. Gorte *Chem Rev*. **1995**, *95*, 615-635.
[52] A. I. M. Rabee, G. A. H. Mekhemer, A. Osatiashtiani, M. A. Isaacs, A. F. Lee, K. Wilson, M. I. Zaki *Catalysts* **2017**, *7*, 204.
[53] X. Zhang, L. J. Durndell, M. A. Isaacs, C. M. A. Parlett, A. F. Lee, K. Wilson *ACS Catal*. **2016**, *6*, 7409-7417.

[54] R. A. Van Santen *Accounts of Chemical Research*. **2009**, *42*, 57-66.
[55] P. M. Mortensen, J. D. Grunwaldt, P. A. Jensen, A. D. Jensen *Catalysis Today*. **2016**, *259*, 277-284.
[56] M. Misono in *Chapter 2 - Chemistry and Catalysis of Mixed Oxides, Vol. 176* (Ed. M. Misono), Elsevier, **2013**, pp.25-65.
[57] V. V. Pushkarev, K. J. An, S. Alayoglu, S. K. Beaumont, G. A. Somorjai *Journal of Catalysis*. **2012**, *292*, 64-72.
[58] K. M. Bratlie, H. Lee, K. Komvopoulos, P. D. Yang, G. A. Somorjai *Nano Lett*. **2007**, *7*, 3097-3101.
[59] L. J. Durndell, G. Zou, W. Shangguan, A. F. Lee, K. Wilson *ChemCatChem*. **2019**, *11*, 3927-3932.
[60] D. Y. Murzin *Catalysis Letters*. **2019**.
[61] L. Dong, L.-L. Yin, Q. Xia, X. Liu, X.-Q. Gong, Y. Wang *Catalysis Science & Technology*. **2018**, *8*, 735-745.
[62] P. M. Mortensen, J. D. Grunwaldt, P. A. Jensen, A. D. Jensen *ACS Catal*. **2013**, *3*, 1774-1785.
[63] C. A. Teles, R. C. Rabelo-Neto, J. R. de Lima, L. V. Mattos, D. E. Resasco, F. B. Noronha *Catalysis Letters*. **2016**, *146*, 1848-1857.
[64] J. K. Nørskov, J. Rossmeisl, A. Logadottir, L. Lindqvist, J. R. Kitchin, T. Bligaard, H. Jónsson *The Journal of Physical Chemistry B*. **2004**, *108*, 17886-17892.
[65] H. Sachdeva, D. Dwivedi, R. Bhattacharjee, S. Khaturia, R. Saroj *Journal of Chemistry*. **2012**, *2013*.
[66] B. Palakshi Reddy, P. Iniyavan, S. Sarveswari, V. Vijayakumar *Chinese Chemical Letters*. **2014**, *25*, 1595-1600.
[67] R. Azhagu Raj, S. M. AlSalhi, S. Devanesan *Materials*. **2017**, *10*.
[68] G. Li, J. Han, H. Wang, X. Zhu, Q. Ge *ACS Catal*. **2015**, *5*, 2009-2016.
[69] R. Réocreux, C. A. Ould Hamou, C. Michel, J. B. Giorgi, P. Sautet *ACS Catal*. **2016**, *6*, 8166-8178.
[70] H. Ohta, H. Kobayashi, K. Hara, A. Fukuoka *Chem Commun*. **2011**, *47*, 12209-12211.
[71] W. J. Song, Y. S. Liu, E. Barath, C. Zhao, J. A. Lercher *Green Chemistry*. **2015**, *17*, 1204-1218.
[72] E. Furimsky *Appl Catal a-Gen*. **2000**, *199*, 147-190.
[73] U. Sanyal, Y. Song, N. Singh, J. L. Fulton, J. Herranz, A. Jentys, O. Y. Gutiérrez, J. A. Lercher *ChemCatChem*. **2019**, *11*, 575-582.
[74] J. Resasco, F. Yang, T. Mou, B. Wang, P. Christopher, D. E. Resasco *ACS Catal*. **2020**, *10*, 595-603.
[75] S. Qiu, Y. Xu, Y. Weng, L. Ma, T. Wang *Catalysts*. **2016**, *6*.
[76] K. Li, R. Wang, J. Chen *Energy & Fuels*. **2011**, *25*, 854-863.
[77] H. Taghvaei, M. R. Rahimpour, P. Bruggeman *RSC Advances*. **2017**, *7*, 30990-30998.
[78] K. Wang, X. Dong, Z. Chen, Y. He, Y. Xu, Z. Liu *Microporous and Mesoporous Materials*. **2014**, *185*, 61-65.
[79] D. Shi, J. M. Vohs *Journal of Physics: Energy*. **2018**, *1*, 015003.
[80] K. D. Rendulic, B. A. Sexton *Journal of Catalysis*. **1982**, *78*, 126-135.
[81] Y. P. Tan, S. Khatua, S. J. Jenkins, J. Q. Yu, J. B. Spencer, D. A. King *Surface Science*. **2005**, *589*, 173-183.
[82] R. L. Burwell Jr *Chem Rev*. **1954**, *54*, 615-685.

[83] Q. Meng, M. Hou, H. Liu, J. Song, B. Han *Nat Commun*. **2017**, *8*, 14190.
[84] M. Siskin, G. Brons, S. N. Vaughn, A. R. Katritzky, M. J. E. Balasubramanian, Fuels *Energy & Fuels*. **1990**, *4*, 488-492.
[85] T. W. van Deelen, C. Hernández Mejía, K. P. de Jong *Nature Catalysis*. **2019**, *2*, 955-970.
[86] T. O. Omotoso, B. Baek, L. C. Grabow, S. P. Crossley *ChemCatChem*. **2017**, *9*, 2642-2651.
[87] A. Pulido, B. Oliver-Tomas, M. Renz, M. Boronat, A. Corma *ChemSusChem*. **2013**, *6*, 141-151.
[88] E. L. Margelefsky, R. K. Zeidan, M. E. Davis *Chemical Society Reviews*. **2008**, *37*, 1118-1126.
[89] Y. Zhang, B. S. Takale, F. Gallou, J. Reilly, B. H. Lipshutz *Chemical Science*. **2019**, *10*, 10556-10561.
[90] G. Liu, A. W. Robertson, M. M.-J. Li, W. C. H. Kuo, M. T. Darby, M. H. Muhieddine, Y.-C. Lin, K. Suenaga, M. Stamatakis, J. H. Warner, S. C. E. Tsang *Nature Chemistry*. **2017**, *9*, 810-816.